Contents

1. Materials and Methods

1.1. Synthesis of single-crystal MAPbBr3 thin films

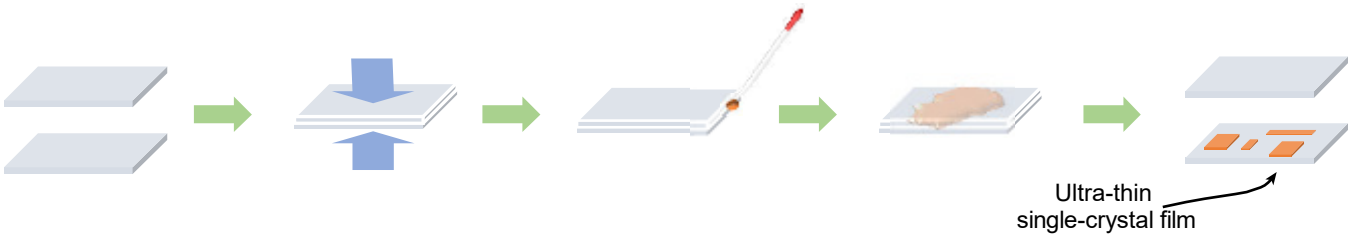

Fig. S1 | Synthesize of single-crystal $MAPbBr_3$ thin films. Single-crystal $MAPbBr_3$ thin films are synthesized using a space-confined method. First, a precursor solution is prepared by dissolving high-purity (99.99%) MABr and $PbBr_2$ powders in DMF at a 1:1 molar ratio, with the concentration adjusted to 0.5 mol/L. Second, two ultrasonically cleaned substrates are clamped together under external stress to form a tightly confined assembly. Third, the precursor solution is dispensed at the edge of this assembly and drawn into the gap by capillary action. Forth, crystallization proceeds at 40°C for over 24 hours in a controlled environment. Finally, after solvent evaporation, the substrates are separated to retrieve the resulting single-crystal $MAPbBr_3$ thin films.

The $MAPbBr_3$ single crystal films are synthesized using an optimized space-confined method. We employ a physical confinement approach to synthesize $MAPbBr_3$ single crystals. The process begins with preparing precursor solution by dissolving high-purity (99.99%) MABr and $PbBr_2$ powders in dimethyl formamide solvent at a 1:1 molar ratio. The solution is adjusted to 0.5 mol/L. In parallel, two ultrasonically cleaned quartz substrates are clamped together under external stress to form a tightly confined assembly. The precursor solution is then dispensed onto the edge of this assembly and drawn into the narrow gap by capillary action. Crystallization proceeds at 40 °C for over 24 hours in a controlled environment. After solvent evaporation, the substrates are separated to retrieve the resulting single-crystal $MAPbBr_3$ thin films.

1.2. Fabrication of photonic crystals

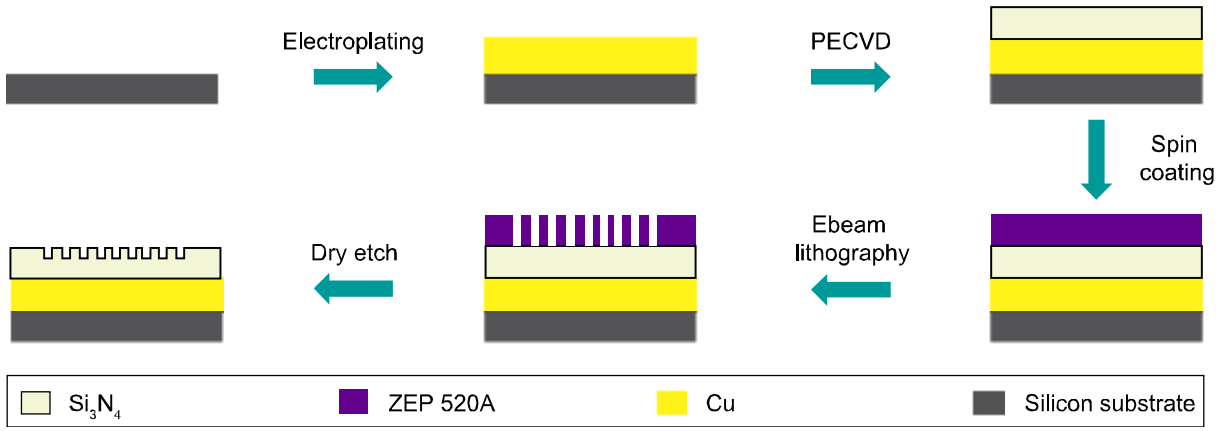

Fig. S2 | Fabrication process of photonic crystals. A 2-μm-thick copper sacrificial layer is first electroplated onto a silicon substrate. Next, a 250-nm-thick Si_3N_4 layer is deposited by plasma-enhanced chemical vapor deposition (PECVD). A 200-nm-thick layer of electron-beam resist ZEP 520A is then spin-coated onto the surface. Photonic crystal patterns are defined via electron-beam lithography and subsequently transferred into the Si_3N_4 layer by dry etching.

Firstly, 250-nm-thick Si_3N_4 is deposited on a 2-μm-thick copper sacrificial layer on the silicon substrate using plasma enhanced chemical vapor deposition (PECVD) method. After that, electron-beam lithography is performed on 200-nm-thick electron-beam resist ZEP 520A to define the photonic crystal patterns. These patterns are further transferred to the Si_3N_4 layer by dry etching. Next, the prepared photonic crystal is placed in a 99% $FeCl_3$ solution for wet etching, and after the copper sacrificial layer has been completely etched, the Si_3N_4 photonic crystals are released and then transferred to a PDMS stamp mounted on a high-precision piezo-stage for following measurements.

1.3. Damage-free integration of $MAPbBr_3$ onto photonic crystals

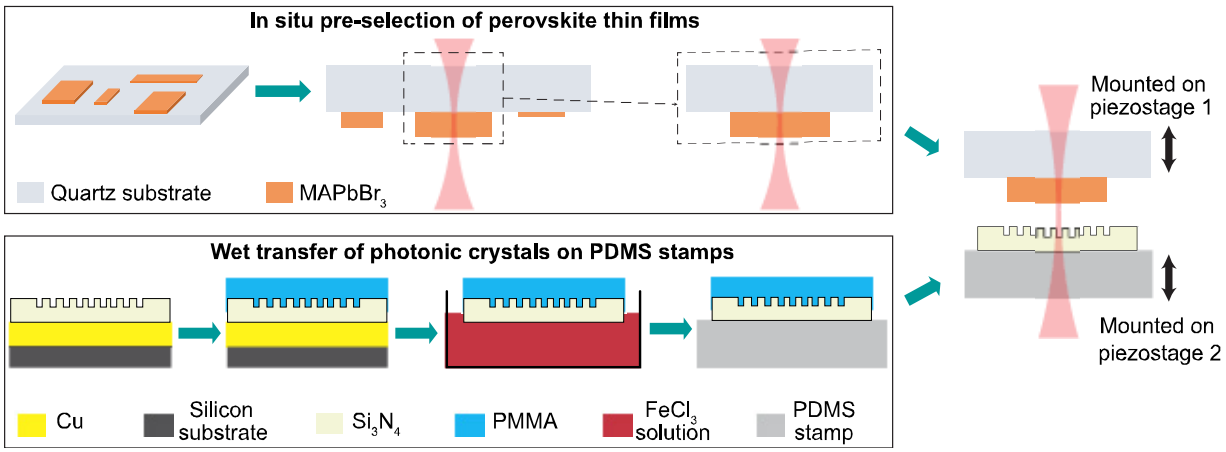

Fig. S3 | Schematic of the damage-free integration method. A perovskite film is pre-selected by *in situ* thickness measurement, and a photonic crystal is transferred via a soft PDMS stamp for gentle assembly.

Conventional methods for fabricating photonic nanostructures in perovskite films, such as focused ion beam milling and inductive plasmas etching, inevitably introduce nonradiative defects that degrade optical performance. To address these issues, we implement a damage-free integration method combining *in situ* thickness pre-selection with micro-transfer printing. We begin by mounting the as-synthesized perovskite films onto a 3D piezo-stage within our momentum-resolved micro-spectroscopy setup. The film thickness is determined *in situ* by fitting the measured transmission spectra, allowing us to select perovskite samples that match the target thickness. The Si_3N_4 photonic crystals are fabricated by standard electron-beam lithography and subsequent dry etching. Beneath the Si_3N_4 layer, a copper sacrificial layer serves to minimize charging effects during lithography and subsequently enables the release of the structures via wet etching in an $FeCl_3$ solution. Once released, the photonic crystals are transferred onto a soft PDMS stamp affixed to a high-precision piezo-stage. This stamp allows for gentle and precise alignment with the pre-selected perovskite films, ensuring damage-free integration. Furthermore, the weak adhesion at the Si_3N_4–perovskite interface allows reversible contact and detachment, providing exceptional flexibility during device assembly and optimization. Collectively, these steps establish a straightforward, reliable, and versatile pathway to realizing high-performance hybrid polariton devices.

1.4. Characterization setup

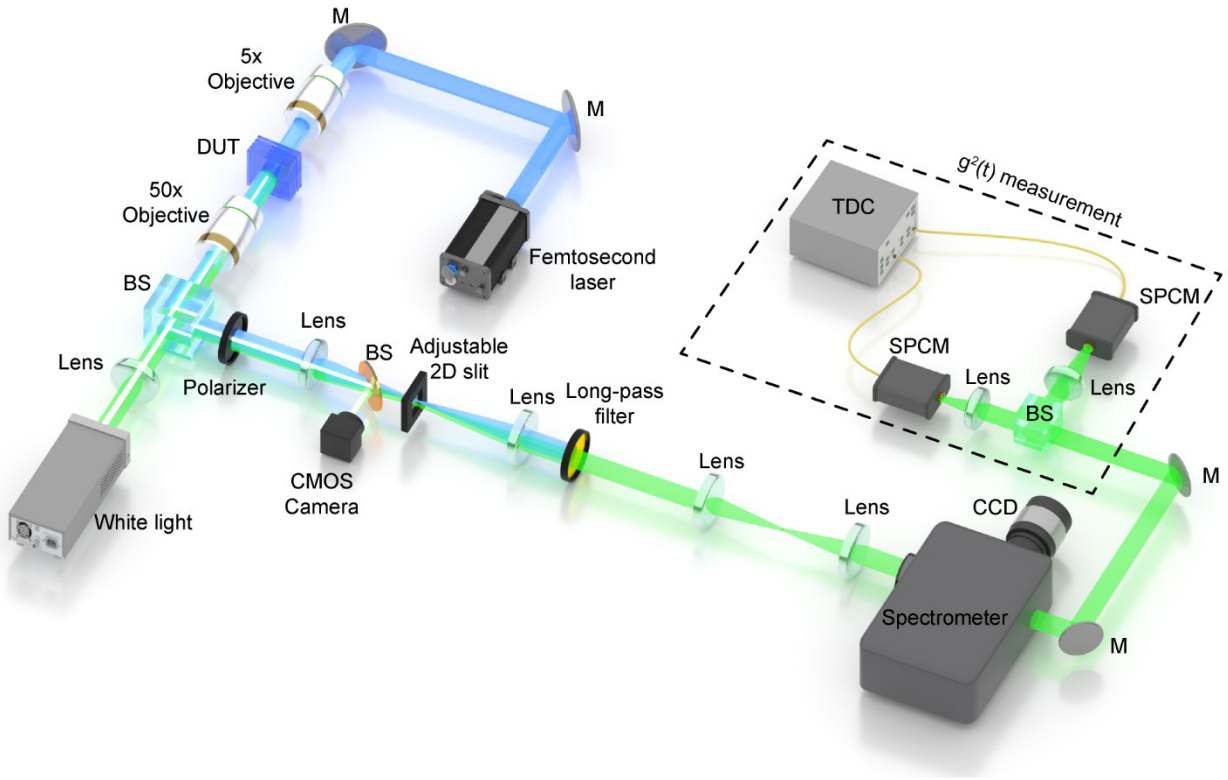

Fig. S4 | Schematic of characterization setup. A femtosecond pump laser (repetition rate = 1 MHz, λ = 500 nm) is focused by a 5× objective to a spot with diameter of 20 μm on the sample. A halogen lamp provides broadband illumination for reflectance measurements. Emission and reflection signals are collected via a 50× objective. For angle-resolved spectroscopy, the spectrometer entrance slit is placed at the Fourier plane. An adjustable two-dimensional slit at the real-space image plane provides spatial filtering, and a 514 nm long-pass filter blocks the pump laser. Second-order quantum coherence is acquired using a Hanbury-Brown-Twiss (HBT) setup, where two fiber-coupled single-photon counting modules measure quantum correlations between arbitrary points in momentum space. (BS: beamsplitter, M: mirror, SPCM: single photon counting module, TDC: time-to-digital converter, DUT: device under test)

A home-built microscope is used to enable real-space and momentum-space resolved spectroscopy and imaging. The emission from the microcavity is collected using a 50× objective and then sent to a monochromator (Princeton Instruments Acton 2300i) with a liquid nitrogen–cooled charge-coupled device camera (Princeton Instruments, PIXIS-100B). The excitation source is a 500-nm non-resonant

pulsed laser (pulse duration: 100 fs, repetition rate: 80 MHz). The repetition rate of the laser is further reduced to 1 MHz by a pulse picker to reduce the heat effect. Second-order quantum coherence is acquired using a HBT setup, where two fiber-coupled single-photon counting modules measure quantum correlations between arbitrary points in momentum space.

2. Theoretical modeling of multi-mode exciton–polariton photonic crystals

2.1. Multi-mode photonic crystals and BIC resonance

This section develops a theoretical model for multi-mode photonic crystals, considering only the photonic degrees of freedom and excluding light-matter interactions with excitons.

We analyze a system of $N_{ph} = 4$ guided modes, consisting of counter-propagating fundamental modes and first-order modes. Their dynamics are governed by the Hamiltonian:

$$\mathbf{H}_{ph}(\mathbf{k}) = \mathbf{H}_0(\mathbf{k}) + i\boldsymbol{\Gamma}_0(\mathbf{k}), \tag{S1}$$

where $\mathbf{H}_0(\mathbf{k})$ is the Hermitian part and $\boldsymbol{\Gamma}_0(\mathbf{k})$ describes radiative losses. The explicit form of $\mathbf{H}_0(\mathbf{k})$ is:

$$\mathbf{H}_0(\mathbf{k}) = \begin{bmatrix} \omega_0 + \frac{c}{n_g}k_x & U_0 & U_{0,1} & 0 \\ U_0 & \omega_0 - \frac{c}{n_g}k_x & 0 & U_{0,1} \\ U_{0,1} & 0 & \omega_1 + \frac{c}{n_g}k_x & U_1 \\ 0 & U_{0,1} & U_1 & \omega_1 - \frac{c}{n_g}k_x \end{bmatrix} + \frac{ca}{4\pi n_g}k_y^2. \tag{S2}$$

Here, ω_0 and ω_1 are the resonant frequencies of fundamental and first-order modes at the Brillouin zone center ($k_x = k_y = 0$), n_g is the group index, and a is the lattice constant. The couplings U_0 and U_1 describe the interaction between counter-propagating modes of the same mode order, while $U_{0,1}$ arises from broken inversion symmetry along the z-direction and couples the modes of different orders.

The dissipative matrix is:

$$\boldsymbol{\Gamma}(\mathbf{k}) = \begin{bmatrix} \gamma_0 & \gamma_0 \cdot \delta & 0 & 0 \\ \gamma_0 \cdot \delta & \gamma_0 & 0 & 0 \\ 0 & 0 & \gamma_1 & \gamma_1 \cdot \delta \\ 0 & 0 & \gamma_1 \cdot \delta & \gamma_1 \end{bmatrix}, \tag{S3}$$

where γ_0 and γ_1 are the radiative loss rates for the fundamental and first-order modes, respectively. The momentum-dependent coefficient

$$\delta(\mathbf{k}) = \frac{k_x^2 + k_y^2 - (2\pi/a)^2}{\sqrt{\left[k_x^2 + k_y^2 + (2\pi/a)^2\right]^2 - (4\pi k_x/a)^2}}$$

describes the non-Hermitian coupling between counter-propagating modes. These terms are essential for forming photonic bound states in the continuum (BIC), which theoretically exhibits vanishing radiation loss.

The photonic mode dispersion is obtained by diagonalizing $\mathbf{H}_{ph}(\mathbf{k})$:

$$\omega_{m,s}(\mathbf{k})\left|a_{m,s}(\mathbf{k})\right\rangle = [\mathbf{H}_0(\mathbf{k}) + i\boldsymbol{\Gamma}(\mathbf{k})]\left|a_{m,s}(\mathbf{k})\right\rangle, \tag{S4}$$

where m labels the fundamental ($m = 0$) and first-order ($m = 1$) modes, and $s = \pm 1$ corresponds to standing-wave resonance with odd and even symmetry along the x-direction. The corresponding photonic eigenstates are $\left|a_{m,s}(\mathbf{k})\right\rangle$.

In the special case of $U_{0,1} = 0$, the eigenvalues are

$$\omega_{m,s}(\mathbf{k}) = \omega_m + \frac{ca}{4\pi n_g}k_y^2 + i\gamma_m + s\cdot\sqrt{\left(c/n_g\right)^2 k_x^2 + \left(U_m + i\gamma_m\cdot\delta(\mathbf{k})\right)^2}.$$

At the Brillouin zone center, BIC modes have purely real eigenfrequencies $\omega_{m,s=-1}(\mathbf{k} = \mathbf{0}) = \omega_m - U_m$, confirming their ultra-high Q factors.

In the general case with $U_{0,1} \neq 0$, the four photonic bands $\omega_{m,s}(\mathbf{k})$ are obtained by numerically solving the 4×4 eigenvalue problem of the full photonic Hamiltonian. The nonzero $U_{0,1}$ weakly couples the fundamental and first-order modes, so that the Bloch modes $\left|a_{m,s}(\mathbf{k})\right\rangle$ to comprise both fundamental and first-order waveguide modes. However, $U_{0,1}$ does not mix the Bloch modes $\left|a_{m,s}(\mathbf{k})\right\rangle$ because they remain mutually orthogonal.

2.2. Multi-mode exciton–polaritons

This section develops a model for the strong coupling between multi-mode photonic bands and excitonic resonances.

We consider the perovskite to exhibit N_{ex}-fold degenerate excitonic resonances at frequency ω_{ex}. Since the lattice constant of the excitonic material is orders-of-magnitude smaller than that of the photonic crystal, the free exciton dispersions are densely folded into the first Brillouin zone, resulting in $N_{ex} >> N_{ph}$. Consequently, the excitonic mode basis can be chosen such that the i-th excitonic mode couples exclusively to the i-th photonic mode for $1 \le i \le N_{ph}$, while the remaining "dark" excitonic modes ($N_{ph} + 1 \le i \le N_{ex}$) remain completely decoupled from the photonic modes. We define four excitonic modes $|b_{m,s}(\mathbf{k})\rangle$ that couple to the four photonic modes $|a_{m,s}(\mathbf{k})\rangle$ respectively. The full exciton–polariton Hamiltonian is a $2N_{ph} \times 2N_{ph}$ matrix $\mathbf{H}(\mathbf{k})$ acting on the combined space of N_{ph} photonic and excitonic modes:

$$\mathbf{H}(\mathbf{k}) = \begin{bmatrix} \mathbf{H}_{ph}(\mathbf{k}) & g\mathbf{I} \\ g\mathbf{I} & (\omega_{ex} + i\gamma_{ex})\mathbf{I} \end{bmatrix}, \tag{S5}$$

where $\mathbf{I}_{N_{ph}}$ is the $N_{ph} \times N_{ph}$ identity matrix. For simplicity, we assume a constant light–matter interaction strength g between each photonic mode $|a_{m,s}(\mathbf{k})\rangle$ and its corresponding excitonic mode $|b_{m,s}(\mathbf{k})\rangle$.

Diagonalization of the Hamiltonian in Eq. (S5) yields eight polariton eigenstates $|\psi_{m,s,p}(\mathbf{k})\rangle$:

$$\begin{cases} |\psi_{m,s,p=1}(\mathbf{k})\rangle = \cos(\theta_{m,s}/2)|a_{m,s}(\mathbf{k})\rangle + \sin(\theta_{m,s}/2)|b_{m,s}(\mathbf{k})\rangle \\ |\psi_{m,s,p=-1}(\mathbf{k})\rangle = -\sin(\theta_{m,s}/2)|a_{m,s}(\mathbf{k})\rangle + \cos(\theta_{m,s}/2)|b_{m,s}(\mathbf{k})\rangle \end{cases}. \tag{S6}$$

Here, m denotes the fundamental ($m = 0$) and first-order ($m = 1$) modes, $s = \pm 1$ represents standing-wave resonances with odd and even symmetry along the x direction, and $p = \pm 1$ labels to the lower and upper polariton branches, respectively. The mixing angle $\theta_{m,s}$ in Eq. (S6) is defined as:

$$\tan\theta_{m,s} = \frac{2g}{\omega_{m,s} - \omega_{ex} + i(\gamma_m - \gamma_{ex})}.$$

The corresponding eigenvalues are:

$$\omega_{m,s,p}(\mathbf{k}) = \frac{\omega_{m,s} + \omega_{ex} + i\gamma_{ex}}{2} + p\sqrt{\left(\frac{\omega_{m,s} - \omega_{ex} - i\gamma_{ex}}{2}\right)^2 + g^2}, \quad \text{(S7)}$$

The band structure of the system calculated using Eq. (S7) is shown in Fig. 1b.

3. Theoretical analysis of polariton supersolids

3.1. Nonlinear interactions of multi-mode exciton–polaritons

This section models nonlinear polariton interactions. We consider repulsive exciton-exciton interaction in real space:

$$\widehat{V} = \int \mu_0 \left| \left\langle \sum_{m,s} b_{m,s}(\mathbf{r}) \,\middle|\, \sum_{m,s} b_{m,s}(\mathbf{r}) \right\rangle \right|^2 d\mathbf{r}.$$

Transforming into momentum space yields the nonlinear interaction:

$$\widehat{V} = \sum_{\{m_i\},\{s_i\}} \iiint \mu_0 \left\langle b_{m_1,s_1}(\mathbf{k}_1) \middle| b_{m_2,s_2}(\mathbf{k}_2) \right\rangle \left\langle b_{m_3,s_3}(\mathbf{k}-\mathbf{k}_1) \middle| b_{m_4,s_4}(\mathbf{k}-\mathbf{k}_2) \right\rangle d\mathbf{k}_1 d\mathbf{k}_2 d\mathbf{k}\,.$$

According to Eq. (S6), the exciton operators can be expressed in terms of polariton operators:

$$\left| b_{m,s}(\mathbf{k}) \right\rangle = \sin\left(\theta_{m,s}/2\right) \left| \psi_{m,s,1}(\mathbf{k}) \right\rangle + \cos\left(\theta_{m,s}/2\right) \left| \psi_{m,s,-1}(\mathbf{k}) \right\rangle.$$

In our study, we consider only the two lowest exciton-polariton branches, defined as $\widehat{\psi}_m(\mathbf{k}) = \left| \psi_{m,-1,-1}(\mathbf{k}) \right\rangle$ (with m = 0, 1). Neglecting higher polariton branches, we obtain:

$$\widehat{V} = \sum_{\{m_i\}} \iiint \alpha_{\{m_i\}}(\mathbf{k}_1, \mathbf{k}_2, \mathbf{k}) \widehat{\psi}^{\dagger}_{m_1}(\mathbf{k}_1) \widehat{\psi}_{m_2}(\mathbf{k}_2) \widehat{\psi}^{\dagger}_{m_3}(\mathbf{k}-\mathbf{k}_1) \widehat{\psi}_{m_4}(\mathbf{k}-\mathbf{k}_2) d\mathbf{k}_1 d\mathbf{k}_2 d\mathbf{k}\,, \tag{S8}$$

where the nonlinear interaction coefficient is:

$$\alpha_{\{m_i\}} = \mu_0 \cos\left[\frac{\theta_{m_1,-1}(\mathbf{k}_1)}{2}\right] \cos\left[\frac{\theta_{m_2,-1}(\mathbf{k}_2)}{2}\right] \times \cos\left[\frac{\theta_{m_3,-1}(\mathbf{k}-\mathbf{k}_1)}{2}\right] \cos\left[\frac{\theta_{m_4,-1}(\mathbf{k}-\mathbf{k}_2)}{2}\right]. \tag{S9}$$

We now consider the special case where a macroscopic number of particles condense into a BEC at the zero-momentum in the fundamental mode $\psi_0(\mathbf{k}=0) = \left| \psi_{0,-1,-1}(\mathbf{k}=0) \right\rangle$, which corresponds to a high-Q BIC resonance. In this regime, the BEC field can be treated as a coherent field $\psi_0 = \sqrt{n_0} \cdot \exp\left(i\varphi_0\right)$, while the finite-momentum components of the fundamental mode $\psi_0(\mathbf{k} \neq 0)$ can be neglected.

Focusing on quantum fluctuations of the first-order mode $\psi_1(\mathbf{k})$, the nonlinear interaction in Eq. (S8) decomposes into three parts: $\widehat{V} = V_0 + \widehat{V}_1 + \widehat{V}_2$. The first term, $V_0 = 2\alpha_0 \cdot n_0^2$, represents the self-repulsion blueshift of the BEC mode, with $\alpha_0 = \mu_0 \cos^4\left[\theta_{0,-1}(0)/2\right]$. The second term,

$$\hat{V}_1 = \int 4\alpha_1 n_0 \cdot \hat{\psi}_1^\dagger(\mathbf{k})\hat{\psi}_1(\mathbf{k}) + \alpha_1 n_0 \cdot \left[e^{2i\varphi_0}\hat{\psi}_1^\dagger(\mathbf{k})\hat{\psi}_1^\dagger(-\mathbf{k}) + h.c.\right]d\mathbf{k} \tag{S10}$$

describes interactions of first-order mode, where $\alpha_1 = \mu_0 \cos^2\left[\theta_{0,-1}(0)/2\right]\cos^2\left[\theta_{1,-1}(\mathbf{k})/2\right]$. The first term in Eq. (S10) gives the blueshift of the $\hat{\psi}_1(\mathbf{k})$ state induced by polariton BEC, while the remaining terms represent squeezing interactions between $\hat{\psi}_1(\mathbf{k})$ and $\hat{\psi}_1(-\mathbf{k})$. Finally, the term

$$\hat{V}_2 = \iiint \alpha(\mathbf{k}_1, \mathbf{k}_2, \mathbf{k}) \cdot \hat{\psi}_1^\dagger(\mathbf{k}_1)\hat{\psi}_1(\mathbf{k}_2)\hat{\psi}_1^\dagger(\mathbf{k}-\mathbf{k}_1)\hat{\psi}_1(\mathbf{k}-\mathbf{k}_2)d\mathbf{k}_1 d\mathbf{k}_2 d\mathbf{k}\,, \tag{S11}$$

Accounts for the self-repulsion energy of the $\hat{\psi}_1(\mathbf{k})$ mode, which can be neglected below the supersolid formation threshold.

3.2. Threshold for the emergent supersolid phase

Unlike BECs and supersolids in ultracold atomic systems, exciton–polaritons inherently exhibit finite lifetimes due to radiative and non-radiative dissipation. The dynamics of this open quantum system at finite temperature are modeled using a Lindblad master equation.

The density matrix $\hat{\rho}$ of the first-order mode $\widehat{\psi}_1(\mathbf{k})$ evolves according to

$$\frac{d\hat{\rho}}{dt} = -i\left[\sum_{\mathbf{k}} \widehat{H}_{\mathbf{k}}, \hat{\rho}\right] + \sum_{\mathbf{k}} (n_{th}+1)\Gamma_{\mathbf{k}} \mathbb{D}\left[\widehat{\psi}_1(\mathbf{k})\right]\hat{\rho} + \sum_{\mathbf{k}} n_{th}\Gamma_{\mathbf{k}} \mathbb{D}\left[\widehat{\psi}_1^{\dagger}(\mathbf{k})\right]\hat{\rho}, \tag{S12}$$

where n_{th} denotes the thermal population of the bath, and the Lindblad dissipator is:

$$\mathbb{D}\left[\widehat{X}\right]\hat{\rho} = \widehat{X}\hat{\rho}\widehat{X}^{\dagger} - \frac{1}{2}\left(\widehat{X}^{\dagger}\widehat{X}\hat{\rho} + \hat{\rho}\widehat{X}^{\dagger}\widehat{X}\right). \tag{S13}$$

Note that spontaneous photoluminescence of $\widehat{\psi}_1(\mathbf{k})$ mode from the exciton reservoir is neglected for simplicity. In Eq. (S12), $\Gamma_{\mathbf{k}} = \mathrm{Im}\left[\omega_{1,-1,-1}(\mathbf{k})\right]$ is the decay rate of polariton mode, and the second-quantized Hamiltonian is:

$$\widehat{H}_{\mathbf{k}} = \frac{\Delta_{\mathbf{k}}}{2}\widehat{\psi}_1^{\dagger}(\mathbf{k})\widehat{\psi}_1(\mathbf{k}) + \frac{\Delta_{-\mathbf{k}}}{2}\widehat{\psi}_1^{\dagger}(-\mathbf{k})\widehat{\psi}_1(-\mathbf{k}) + \alpha_1 n_0 e^{2i\varphi_0}\widehat{\psi}_1^{\dagger}(\mathbf{k})\widehat{\psi}_1^{\dagger}(-\mathbf{k}) + h.c.. \tag{S14}$$

Here, $\Delta_{\mathbf{k}} = \Delta_{-\mathbf{k}}$ is the energy detuning of the $\widehat{\psi}_1(\pm\mathbf{k})$ mode relative to the polariton BEC:

$$\Delta_{\mathbf{k}} = \mathrm{Re}\left[\omega_{1,-1,-1}(\mathbf{k}) + 4\alpha_1 n_0\right] - \mathrm{Re}\left[\omega_{0,-1,-1}(0) + 2\alpha_0 n_0\right]. \tag{S15}$$

The difference in blueshift between the $\widehat{\psi}_1(\mathbf{k})$ mode and the BEC mode reflects the distinction between cross-phase and self-phase modulation in an optical Kerr nonlinear process.

Since the squeezing term in Eq. (S14) breaks particle-number conservation, we apply a Bogoliubov transformation, doubling the degrees of freedom by grouping the annihilation and creation into a vector $|\hat{\mathbf{c}}(\mathbf{k})\rangle = \left[\widehat{\psi}_1(\mathbf{k}),\ \widehat{\psi}_1(-\mathbf{k}), \widehat{\psi}_1^{\dagger}(\mathbf{k}), \widehat{\psi}_1^{\dagger}(-\mathbf{k})\right]^{\mathrm{T}}$. Using Eqs. (S12)–(S15), the classical values $|\bar{\mathbf{c}}(\mathbf{k})\rangle = \left[\langle\widehat{\psi}_1(\mathbf{k})\rangle,\ \langle\widehat{\psi}_1(-\mathbf{k})\rangle, \langle\widehat{\psi}_1^{\dagger}(\mathbf{k})\rangle, \langle\widehat{\psi}_1^{\dagger}(-\mathbf{k})\rangle\right]^{\mathrm{T}}$ (with $\langle\widehat{X}\rangle = \mathrm{tr}\left(\hat{\rho}\widehat{X}\right)$) evolves as

$$\frac{d}{dt}|\bar{\mathbf{c}}(\mathbf{k})\rangle = -i\mathbf{M}_{\mathbf{k}}|\bar{\mathbf{c}}(\mathbf{k})\rangle = -i[(\boldsymbol{\sigma}_z \otimes \mathbf{I}_2)\mathbf{H}_{\mathbf{k}} - i\mathbf{I}_4\boldsymbol{\Gamma}_{\mathbf{k}}]|\bar{\mathbf{c}}(\mathbf{k})\rangle. \tag{S16}$$

where $\boldsymbol{\sigma}_z$ is a Pauli matrix encoding bosonic commutation relations, $\mathbf{I}_n$ is the $n\times n$ identity matrix, and $\mathbf{H}_{\mathbf{k}}$ is the 4×4 Bogoliubov-de Gennes Hamiltonian satisfying $\widehat{H}_{\mathbf{k}} = \frac{1}{2}\langle\hat{\mathbf{c}}(\mathbf{k})|\mathbf{H}_{\mathbf{k}}|\hat{\mathbf{c}}(\mathbf{k})\rangle$. The explicit form of $\mathbf{M}_{\mathbf{k}}$ is:

$$\mathbf{M}_{\mathbf{k}} = \begin{bmatrix} \Delta_{\mathbf{k}} - i\Gamma_{\mathbf{k}} & 0 & 0 & \alpha_1 n_0 e^{2i\varphi_0} \\ 0 & \Delta_{-\mathbf{k}} - i\Gamma_{\mathbf{k}} & \alpha_1 n_0 e^{2i\varphi_0} & 0 \\ 0 & -\alpha_1 n_0 e^{-2i\varphi_0} & -\Delta_{\mathbf{k}} - i\Gamma_{\mathbf{k}} & 0 \\ -\alpha_1 n_0 e^{-2i\varphi_0} & 0 & 0 & -\Delta_{-\mathbf{k}} - i\Gamma_{\mathbf{k}} \end{bmatrix}. \tag{S17}$$

Note that $\Delta_{\mathbf{k}} = \Delta_{-\mathbf{k}}$, and the Bogoliubov-de Gennes Hamiltonian exhibits particle-hole symmetry $(\boldsymbol{\sigma}_x \mathbb{K})^\dagger \mathbf{H}_{\mathbf{k}} (\boldsymbol{\sigma}_x \mathbb{K}) = -\mathbf{H}_{\mathbf{k}}$, where $\mathbb{K}$ is complex conjugation. This symmetry persists even in open systems, as $\mathbf{M}_{\mathbf{k}}$ also satisfies $(\boldsymbol{\sigma}_x \mathbb{K})^\dagger \mathbf{M}_{\mathbf{k}} (\boldsymbol{\sigma}_x \mathbb{K}) = -\mathbf{M}_{\mathbf{k}}$. Consequently, the eigenvalue spectrum is symmetric about zero. If $|\bar{\mathbf{c}}(\mathbf{k})\rangle$ is an eigenstate satisfying $\mathbf{M}_{\mathbf{k}} |\bar{\mathbf{c}}(\mathbf{k})\rangle = \Omega_{\mathbf{k}} \mathbf{M}_{\mathbf{k}} |\bar{\mathbf{c}}(\mathbf{k})\rangle$, then $\boldsymbol{\sigma}_x \mathbb{K} |\bar{\mathbf{c}}(\mathbf{k})\rangle$ is also an eigenstate, obeying $\mathbf{M}_{\mathbf{k}} (\boldsymbol{\sigma}_x \mathbb{K} |\bar{\mathbf{c}}(\mathbf{k})\rangle) = -\Omega_{\mathbf{k}} \boldsymbol{\sigma}_x \mathbb{K} |\bar{\mathbf{c}}(\mathbf{k})\rangle$. Therefore, we only need to consider two eigenvalues:

$$\Omega_{\mathbf{k},\pm} = \pm \sqrt{\Delta_{\mathbf{k}}^2 - (\alpha_1 n_0)^2} - i\Gamma_{\mathbf{k}}. \tag{S18}$$

According to Eq. (S18), when $\alpha_1 n_0 > \sqrt{\Gamma_{\mathbf{k}}^2 + \Delta_{\mathbf{k}}^2}$, the eigenvalue $\Omega_{\mathbf{k},+}$ is purely imaginary, and its imaginary part can even turn positive. This indicates that the polariton BEC can drive the corresponding mode into instability. Maximum parametric gain occurs at $\Delta_{\mathbf{k}} = 0$, corresponding to a parametric scattering process that is isoenergetic to the BEC energy. This signals the onset of supersolid formation when the BEC density exceeds the threshold $n_0 > \Gamma_{\mathbf{k}}/\alpha_1$.

3.3. Stabilization of supersolid phase

This section analyzes the stabilization of the supersolid phase above the threshold. In this regime, the self-repulsive interaction term $\hat{\mathbf{V}}_2$ in Eq. (S11) cannot be neglected due to the macroscopic population in the $\hat{\psi}_1(\mathbf{k})$ and $\hat{\psi}_1(-\mathbf{k})$ mode. The dynamics of $\psi_{\mathbf{k}} = \langle\hat{\psi}_1(\mathbf{k})\rangle$ and $\psi_{-\mathbf{k}} = \langle\hat{\psi}_1(-\mathbf{k})\rangle$ are governed by:

$$\begin{cases} \frac{d}{dt}\psi_{\mathbf{k}} = -i\left[\Delta_{\mathbf{k}} - i\Gamma_{\mathbf{k}} + 4\alpha_{\mathbf{k}}\left(\psi_{\mathbf{k}}^*\psi_{\mathbf{k}} + \psi_{-\mathbf{k}}^*\psi_{-\mathbf{k}}\right)\right]\psi_{\mathbf{k}} - i\alpha_1 n_0 e^{2i\varphi_0}\psi_{-\mathbf{k}}^* \\ \frac{d}{dt}\psi_{-\mathbf{k}} = -i\left[\Delta_{\mathbf{k}} - i\Gamma_{\mathbf{k}} + 4\alpha_{\mathbf{k}}\left(\psi_{\mathbf{k}}^*\psi_{\mathbf{k}} + \psi_{-\mathbf{k}}^*\psi_{-\mathbf{k}}\right)\right]\psi_{-\mathbf{k}} - i\alpha_1 n_0 e^{2i\varphi_0}\psi_{\mathbf{k}}^* \end{cases},$$

where $\alpha_{\mathbf{k}} = \mu_0\cos^4\left[\theta_{1,-1}(\mathbf{k})/2\right]$ is the self-repulsive interaction coefficient for the $\psi_{\mathbf{k}}$ mode. Assuming the ansatz $\psi_{\mathbf{k}} = A_{\mathbf{k}}e^{i\varphi_{\mathbf{k}}}$ and $\psi_{-\mathbf{k}} = A_{-\mathbf{k}}e^{i\varphi_{-\mathbf{k}}}$, we obtain:

$$\begin{cases} \frac{d}{dt}A_{\mathbf{k}} = -\Gamma_{\mathbf{k}}A_{\mathbf{k}} + \alpha_1 n_0 A_{-\mathbf{k}}\sin\left(2\varphi_0 - \varphi_{\mathbf{k}} - \varphi_{-\mathbf{k}}\right) \\ \frac{d}{dt}A_{-\mathbf{k}} = -\Gamma_{\mathbf{k}}A_{-\mathbf{k}} + \alpha_1 n_0 A_{\mathbf{k}}\sin\left(2\varphi_0 - \varphi_{\mathbf{k}} - \varphi_{-\mathbf{k}}\right) \\ A_{\mathbf{k}}\frac{d}{dt}\varphi_{\mathbf{k}} = -\Delta_{\mathbf{k}}A_{\mathbf{k}} - 4\alpha_{\mathbf{k}}\left(A_{\mathbf{k}}^2 + A_{-\mathbf{k}}^2\right)A_{\mathbf{k}} + \alpha_1 n_0 A_{-\mathbf{k}}\cos\left(2\varphi_0 - \varphi_{\mathbf{k}} - \varphi_{-\mathbf{k}}\right) \\ A_{-\mathbf{k}}\frac{d}{dt}\varphi_{-\mathbf{k}} = -\Delta_{\mathbf{k}}A_{-\mathbf{k}} - 4\alpha_{\mathbf{k}}\left(A_{\mathbf{k}}^2 + A_{-\mathbf{k}}^2\right)A_{-\mathbf{k}} + \alpha_1 n_0 A_{\mathbf{k}}\cos\left(2\varphi_0 - \varphi_{\mathbf{k}} - \varphi_{-\mathbf{k}}\right) \end{cases}.$$

Due to the symmetry between counter-propagating modes $\psi_{\mathbf{k}}$ and $\psi_{-\mathbf{k}}$, we set $A_{\mathbf{k}} = A_{-\mathbf{k}} = A$ and $\varphi_{\mathbf{k}} + \varphi_{-\mathbf{k}} = 2\varphi$, which yields:

$$\begin{cases} \frac{dA}{dt} = -\Gamma_{\mathbf{k}}A + \alpha_1 n_0 A\sin\left(2\varphi_0 - 2\varphi\right) \\ \frac{d\varphi}{dt}A = \left[-\Delta_{\mathbf{k}} - 8\alpha_{\mathbf{k}}A^2 + \alpha_1 n_0\cos\left(2\varphi_0 - 2\varphi\right)\right]\cdot A \end{cases}. \tag{S19}$$

Although the system is intrinsically non-equilibrium, a quasi-steady-state solution of Eq. (S19) can be found by setting $dA/dt = 0$ and $d\varphi/dt = 0$. When $\alpha_1 n_0 > \sqrt{\Gamma_{\mathbf{k}}^2 + \Delta_{\mathbf{k}}^2}$, the quasi-steady solution is:

$$\begin{cases} A_{\mathbf{k}}^2 = A_{-\mathbf{k}}^2 = \left(\sqrt{\alpha_1^2 n_0^2 - \Gamma_{\mathbf{k}}^2} - \Delta_{\mathbf{k}}\right)/8\alpha_{\mathbf{k}} \\ \varphi_{\mathbf{k}} + \varphi_{-\mathbf{k}} = \sin^{-1}\left(\frac{\Gamma_{\mathbf{k}}}{\alpha_1 n_0}\right) + 2\varphi_0 \end{cases}. \tag{S20}$$

When $\alpha_1 n_0 < \sqrt{\Gamma_{\mathbf{k}}^2 + \Delta_{\mathbf{k}}^2}$, the steady solution is simply $A_{\mathbf{k}} = A_{-\mathbf{k}} = 0$. This analysis clearly characterizes the phase transition from a conventional BEC to an emergent supersolid.

It is interesting to note that Eq. (S20) only governs the total phase $\varphi_{\mathbf{k}} + \varphi_{-\mathbf{k}}$ of the counter-propagating modes. The individual phases are:

$$\begin{cases} \varphi_{\mathbf{k}} = \sin^{-1}\left(\dfrac{\Gamma_{\mathbf{k}}}{\alpha_1 n_0}\right)/2 + \varphi_0 + \chi/2 \\ \varphi_{-\mathbf{k}} = \sin^{-1}\left(\dfrac{\Gamma_{\mathbf{k}}}{\alpha_1 n_0}\right)/2 + \varphi_0 - \chi/2 \end{cases}. \tag{S21}$$

Here, χ is a random phase difference between $\psi_{\mathbf{k}}$ and $\psi_{-\mathbf{k}}$, reflecting the spontaneous breaking of an additional U(1) symmetry during supersolid formation. This phase difference can be directly measured by single-shot experiments, as it takes a random value between 0 and 2π in each realization.

The phase transition from BEC to supersolid can be effectively described within a Ginzburg-Landau framework by the free-energy functional:

$$F(A) = \left(\Delta_{\mathbf{k}}^2 + \Gamma_{\mathbf{k}}^2 - \alpha_1^2 n_0^2\right) \cdot A^2 + 4\alpha_{\mathbf{k}} A^4, \tag{S22}$$

where A defines the supersolid amplitude. Its emergence ($A^2 > 0$) signals spontaneous breaking of continuous translational symmetry, and its coexistence with the polariton BEC background establishes the supersolid phase. Crucially, this effective free energy extends the traditional equilibrium theory by explicitly incorporating dissipation, which raises the transition threshold. Our model successfully captures critical behavior and instability onset.

Notably, the supersolid phase first emerges under the isoenergetic condition $\Delta_{\mathbf{k}} = 0$. According to Eq. (S15), this condition implicitly relates the wavevector $\mathbf{k}$ to the BEC density n_0, implying that the spatial period of the emergent supersolid is tunable—a signature of the non-rigid, adjustable nature of polariton supersolids.

3.4. Influence of spatial confinement

The previous sections studied the ideal polariton supersolid in an infinitely extended polariton BEC. In practice, the finite spatial extent of the pump laser, the photonic crystal, and the resulting condensate creates a confinement potential, which introduces a weak linear coupling between counter-propagating first-order modes $\widehat{\psi}_1(\mathbf{k})$ and $\widehat{\psi}_1(-\mathbf{k})$. This section incorporates this effect into the theoretical model.

We modify the matrix $\mathbf{M}_\mathbf{k}$ in Eq. (S17) to:

$$\mathbf{M}_\mathbf{k} = \begin{bmatrix} \Delta_\mathbf{k} - i\Gamma_\mathbf{k} & \beta e^{i\varphi_{\text{linear}}} & 0 & \alpha_1 n_0 e^{2i\varphi_0} \\ \beta e^{-i\varphi_{\text{linear}}} & \Delta_{-\mathbf{k}} - i\Gamma_\mathbf{k} & \alpha_1 n_0 e^{2i\varphi_0} & 0 \\ 0 & -\alpha_1 n_0 e^{-2i\varphi_0} & -\Delta_\mathbf{k} - i\Gamma_\mathbf{k} & -\beta e^{-i\varphi_{\text{linear}}} \\ -\alpha_1 n_0 e^{-2i\varphi_0} & 0 & -\beta e^{i\varphi_{\text{linear}}} & -\Delta_{-\mathbf{k}} - i\Gamma_\mathbf{k} \end{bmatrix}. \tag{S23}$$

where $\beta e^{i\varphi_{\text{linear}}}$ quantifies the linear coupling between counter-propagating modes induced by a confinement potential—which can arise from the finite spatial extent of the pump or from reflections at the photonic crystal boundaries. According to Eq. (S16), the dynamics of $\psi_\mathbf{k} = \langle\widehat{\psi}_1(\mathbf{k})\rangle$ and $\psi_{-\mathbf{k}} = \langle\widehat{\psi}_1(-\mathbf{k})\rangle$ are governed by:

$$\begin{cases} \frac{d}{dt}\psi_\mathbf{k} = -i\left[\Delta_\mathbf{k} - i\Gamma_\mathbf{k} + 4\alpha_\mathbf{k}\left(\psi_\mathbf{k}^*\psi_\mathbf{k} + \psi_{-\mathbf{k}}^*\psi_{-\mathbf{k}}\right)\right]\psi_\mathbf{k} - i\alpha_1 n_0 e^{2i\varphi_0}\psi_{-\mathbf{k}}^* - i\beta e^{i\varphi_{\text{linear}}}\psi_{-\mathbf{k}} \\ \frac{d}{dt}\psi_{-\mathbf{k}} = -i\left[\Delta_\mathbf{k} - i\Gamma_\mathbf{k} + 4\alpha_\mathbf{k}\left(\psi_\mathbf{k}^*\psi_\mathbf{k} + \psi_{-\mathbf{k}}^*\psi_{-\mathbf{k}}\right)\right]\psi_{-\mathbf{k}} - i\alpha_1 n_0 e^{2i\varphi_0}\psi_\mathbf{k}^* - i\beta e^{-i\varphi_{\text{linear}}}\psi_\mathbf{k} \end{cases},$$

Assuming the ansatz $\psi_\mathbf{k} = A_\mathbf{k} e^{i\varphi_\mathbf{k}}$ and $\psi_{-\mathbf{k}} = A_{-\mathbf{k}} e^{i\varphi_{-\mathbf{k}}}$, we obtain:

$$\begin{cases} \frac{d}{dt}A_\mathbf{k} = -\Gamma_\mathbf{k} A_\mathbf{k} + \alpha_1 n_0 A_{-\mathbf{k}} \sin\left(2\varphi_0 - 2\varphi\right) + \beta A_{-\mathbf{k}} \sin\left(\varphi_{\text{linear}} - \chi\right) \\ \frac{d}{dt}A_{-\mathbf{k}} = -\Gamma_\mathbf{k} A_{-\mathbf{k}} + \alpha_1 n_0 A_\mathbf{k} \sin\left(2\varphi_0 - 2\varphi\right) + \beta A_\mathbf{k} \sin\left(\chi - \varphi_{\text{linear}}\right) \\ \frac{d\varphi_\mathbf{k}}{dt} = -\Delta_\mathbf{k} - 4\alpha_\mathbf{k}\left(A_\mathbf{k}^2 + A_{-\mathbf{k}}^2\right) + \alpha_1 n_0 \frac{A_{-\mathbf{k}}}{A_\mathbf{k}} \cos\left(2\varphi_0 - 2\varphi\right) - \beta \frac{A_{-\mathbf{k}}}{A_\mathbf{k}} \cos\left(\varphi_{\text{linear}} - \chi\right) \\ \frac{d\varphi_{-\mathbf{k}}}{dt} = -\Delta_\mathbf{k} - 4\alpha_\mathbf{k}\left(A_\mathbf{k}^2 + A_{-\mathbf{k}}^2\right) + \alpha_1 n_0 \frac{A_\mathbf{k}}{A_{-\mathbf{k}}} \cos\left(2\varphi_0 - 2\varphi\right) - \beta \frac{A_\mathbf{k}}{A_{-\mathbf{k}}} \cos\left(\chi - \varphi_{\text{linear}}\right) \end{cases} \tag{S24}$$

where $2\varphi = \varphi_\mathbf{k} + \varphi_{-\mathbf{k}}$ and $\chi = \varphi_\mathbf{k} - \varphi_{-\mathbf{k}}$. Exploiting the symmetry between counter-propagating modes $\psi_\mathbf{k}$ and $\psi_{-\mathbf{k}}$, we set $A_\mathbf{k} = A_{-\mathbf{k}} = A$. Comparing the first and second equations in Eq. (S24) for a nonzero solution ($A \neq 0$) gives $\chi = \varphi_{\text{linear}} + m\pi$ ($m = 0, 1, 2\ldots$). Substituting this condition yields:

$$\begin{cases} \dfrac{dA}{dt} = -\Gamma_{\mathbf{k}} A + \alpha_1 n_0 A \sin\left(2\varphi_0 - 2\varphi\right) \\ \dfrac{d\varphi}{dt} A = \left[-\Delta_{\mathbf{k}} - 8\alpha_{\mathbf{k}} A^2 + \alpha_1 n_0 \cos\left(2\varphi_0 - 2\varphi\right) - \beta(-1)^m\right] \cdot A \end{cases} . \tag{S25}$$

Setting $dA/dt = 0$ and $d\varphi/dt = 0$ gives the quasi-steady-state solution:

$$\begin{cases} A_{\mathbf{k}}^2 = A_{-\mathbf{k}}^2 = \left(\sqrt{\alpha_1^2 n_0^2 - \Gamma_{\mathbf{k}}^2} - \Delta_{\mathbf{k}} - \beta(-1)^m\right) / 8\alpha_{\mathbf{k}} \\ \varphi_{\mathbf{k}} = \varphi_0 + \left[\sin^{-1}\left(\dfrac{\Gamma_{\mathbf{k}}}{\alpha_1 n_0}\right) + \varphi_{\text{linear}} + m\pi\right] / 2 \\ \varphi_{-\mathbf{k}} = \varphi_0 + \left[\sin^{-1}\left(\dfrac{\Gamma_{\mathbf{k}}}{\alpha_1 n_0}\right) - \varphi_{\text{linear}} - m\pi\right] / 2 \end{cases} . \tag{S26}$$

Comparing Eq. (S26) with Eqs. (S20) and (S21) reveals two consequences of the linear coupling term. First, it shifts the effective detuning to $\Delta_{\mathbf{k}} + \beta(-1)^m$. Most importantly, it locks the relative phase between the counter-propagating modes, fixing the phase difference to $\chi = \varphi_{\text{linear}} + m\pi$ as dictated by the linear coupling. We note that analogous effects exist in atomic supersolids, which are inherent in finite-size systems. However, they have not prevented the observation of well-behaved collective excitation spectra of supersolids.

4. Additional results

4.1. $MAPbBr_3$ thin films enabling room-temperature polariton BEC

Using the space-confined synthesis approach described in Sec. 1.1, we can obtain single-crystal $MAPbBr_3$ thin films (Fig. S5a) that exhibits excellent uniformity, with a root-mean-square roughness of 0.7 nm over a 100 μm² area (Fig. S5b). The sharp X-ray diffraction peaks in Fig. S5c confirms their high crystallinity.

The optical property of $MAPbBr_3$ is modeled by a Tauc–Lorentz dielectric function

$$\varepsilon(\omega) = \varepsilon_\infty + \varepsilon_{\mathrm{X}}^{\mathrm{TL}}(\omega) + \varepsilon_{\mathrm{BG}}^{\mathrm{TL}}(\omega), \tag{S27}$$

where $\varepsilon_{\mathrm{X}}^{\mathrm{TL}}(\omega)$ and $\varepsilon_{\mathrm{BG}}^{\mathrm{TL}}(\omega)$ describe the dominant X exciton resonance and the above-bandgap absorption, respectively. The imaginary and real components of each Tauc–Lorentz term are

$$\mathrm{Im}\left[\varepsilon_{\mathrm{X/BG}}^{\mathrm{TL}}(\omega)\right] = \frac{1}{\omega}\frac{A\omega_0\gamma\left(\omega-\omega_g\right)^2}{(\omega^2-\omega_0^2)^2+\gamma^2\omega^2}\Theta\left(\omega-\omega_g\right),$$

$$\mathrm{Re}[\varepsilon_{\mathrm{X/BG}}^{TL}(\omega)] = \frac{2}{\pi}\int_0^\infty \frac{\omega_1 \mathrm{Im}[\varepsilon_{\mathrm{X}}^{TL}(\omega_1)]d\omega_1}{\omega^2-\omega_1^2},$$

where A, γ, ω_0, ω_g are oscillation strength, dissipation rate, resonant frequency, and bandgap energy, respectively.

To fit the measured reflectance spectra, we use the transfer matrix method. For normal incidence, the transfer matrix of the j^{th} layer (thickness d_j, complex refractive index $n_j = \sqrt{\varepsilon_j}$ at wavelength λ) is

$$\mathbf{M}_j = \begin{bmatrix} \cos\left(\frac{2\pi}{\lambda}n_j d_j\right) & \frac{i}{n_j}\sin\left(\frac{2\pi}{\lambda}n_j d_j\right) \\ in_j\sin\left(\frac{2\pi}{\lambda}n_j d_j\right) & \cos\left(\frac{2\pi}{\lambda}n_j d_j\right) \end{bmatrix}.$$

The total transfer matrix of the multilayer stack is

$$\mathbf{M} = \prod_j \mathbf{M}_j = \begin{pmatrix} M_{11} & M_{12} \\ M_{21} & M_{22} \end{pmatrix},$$

and the reflection coefficient is

$$r = \frac{n_0 M_{11} + n_0 n_s M_{12} - M_{21} - n_s M_{22}}{n_0 M_{11} + n_0 n_s M_{12} + M_{21} + n_s M_{22}},$$

where n_0 and n_s are the complex refractive indices of the incident medium (vacuum) and the quartz substrate, respectively. Figure S5d shows a height profile of a typical $MAPbBr_3$ film. The fitted real and imaginary components of $\varepsilon(\omega)$ are presented in Fig. S5e, yielding a resonant exciton energy of 2.377 eV.

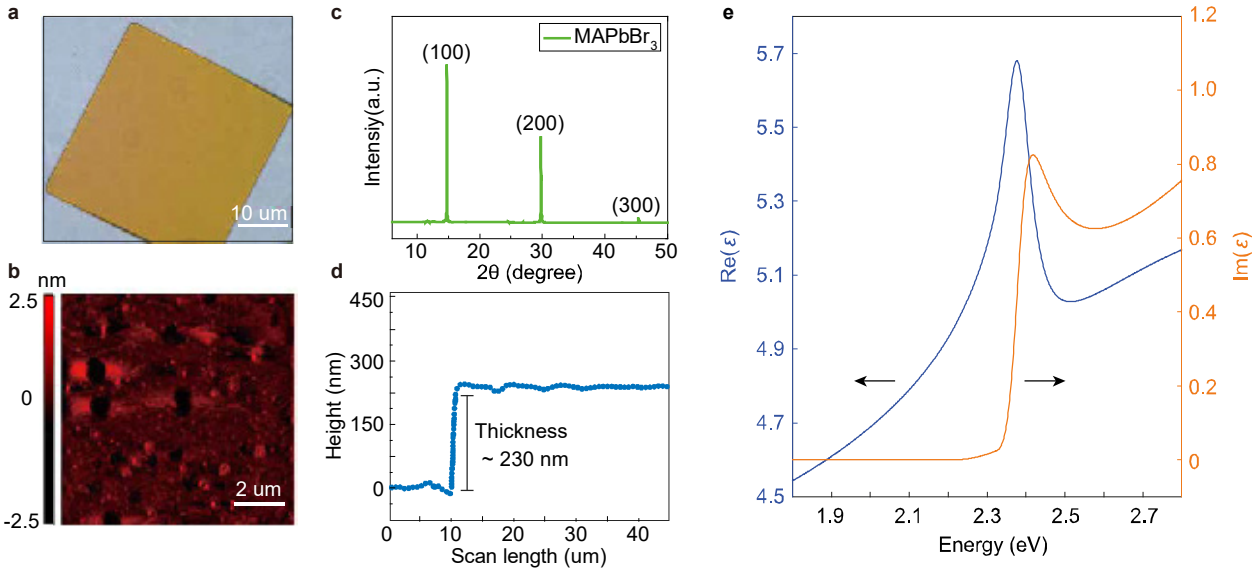

Fig. S5 | Characterization of single-crystal $MAPbBr_3$ thin films. a, Optical micrograph of a single-crystal $MAPbBr_3$ thin film. **b**, Atomic force microscopy image. The root-mean-square roughness is 0.7 nm across a 100 μm² area. **c**, X-ray diffraction pattern of the as-grown single crystals. **d**, Step-profiler height profile of a typical film. **e**, Real and imaginary parts of the permittivity by fitting the transmission spectrum with the Tauc–Lorentz model.

To further confirm the material's suitability for room-temperature BEC, we perform photoluminescence measurements on a distributed Bragg reflector (DBR) cavity integrated with the synthesized perovskite single crystal thin film. As shown in Fig. S6a, the emission intensity shows a pronounced nonlinear increase above a threshold pump intensity. Simultaneously, the linewidth narrows sharply (Fig. S6b), indicating macroscopic occupation of a single quantum state. Angle-resolved spectra collected below, near, and above the threshold (Figs. S6c–e) further confirm the formation of a polariton BEC. These results demonstrate that $MAPbBr_3$ single crystals are capable of supporting high-density polariton condensation at room temperature.

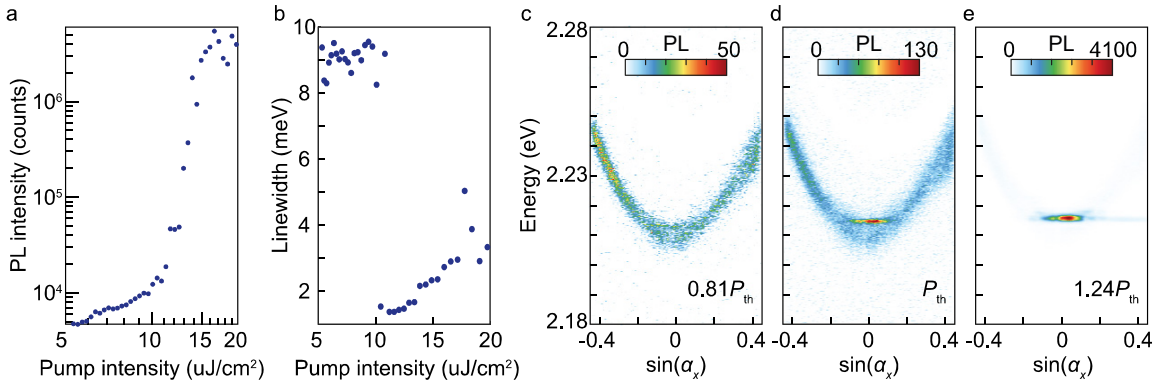

Fig. S6 | Room-temperature polariton BEC in a $MAPbBr_3$-based DBR microcavity.

a, Photoluminescent intensity as a function of pump intensity. **b**, Emission linewidth as a function of pump intensity. **c**–**e**, Angle-resolved photoluminescent spectra measured below (**c**), near (**d**), and above (**e**) the condensation threshold.

4.2. Multi-mode photonic crystals

Figure S7 shows the characterization of the multi-mode photonic crystals before integration with $MAPbBr_3$. The numerically simulated angle-resolved reflection spectrum (Fig. S7a) is calculated using the geometric parameters given in the main text: an Si_3N_4 etch depth t_{etch} = 50 nm on a residual substrate thickness t_{sub} = 200 nm; a lattice constant a = 290 nm; and a duty cycle r = 0.2. The experimentally measured spectrum (Fig. S7b) agrees well with the simulation. In addition, the measured iso-frequency contours at two BIC wavelengths (Figs. S7c and d) show multiple photonic modes surrounding the BIC states. Nall data presented here are for the bare photonic crystals without $MAPbBr_3$. Upon integration with $MAPbBr_3$, the photonic band structure redshifts and exhibits anti-crossing with the exciton resonance of the perovskite.

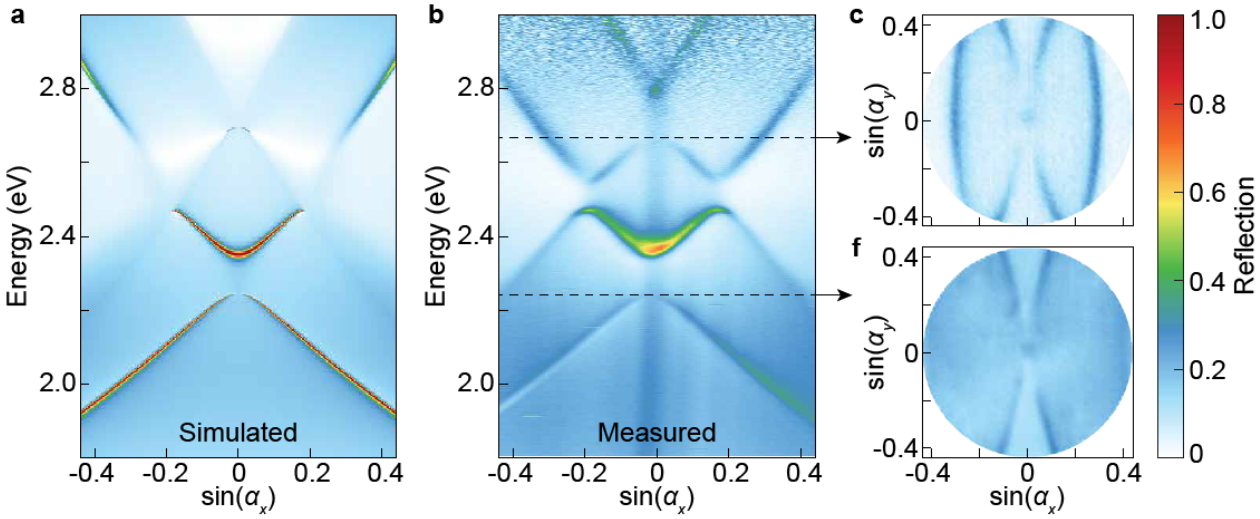

Fig. S7 | Reflectance spectra of the bare photonic crystal without $MAPbBr_3$. a, Simulated band diagram showing multiple photonic modes. **b**, Measured band diagram of the bare photonic crystal. **c** and **d**, Measured iso-frequency contours at the energies of two BIC states. The ideal BIC appears as a dark point; the residual signal at the Γ-point originates from reflection at the back surface of the quartz substrate.